Photodissociation of pyrrole–ammonia clusters by velocity map imaging: mechanism for the H-atom transfer reaction

L. Rubio-Lago,*[ab] G. A. Amaral,[a] A. N. Oldani,[c] J. D. Rodríguez,[a] M. G. González,[a] G. A. Pino[c] and L. Bañares*[a]

Received 6th August 2010, Accepted 12th October 2010
DOI: 10.1039/c0cp01442g

The photodissociation dynamics of pyrrole–ammonia clusters ($PyH\cdot(NH_3)_n$, n = 2–6) has been studied using a combination of velocity map imaging and non-resonant detection of the $NH_4(NH_3)_{n-1}$ products. The excited state hydrogen-atom transfer mechanism (ESHT) is evidenced through delayed ionization and presents a threshold around 236.6 nm, in agreement with previous reports. A high resolution determination of the kinetic energy distributions (KEDs) of the products reveals slow ($\sim$0.15 eV) and structured distributions for all the ammonia cluster masses studied. The low values of the measured kinetic energy rule out the existence of a long-lived intermediate state, as it has been proposed previously. Instead, a direct N–H bond rupture, in the fashion of the photodissociation of bare pyrrole, is proposed. This assumption is supported by a careful analysis of the structure of the measured KEDs in terms of a discrete vibrational activity of the pyrrolyl co-fragment.

I. Introduction

The deactivation pathways of photoexcited biological molecular complexes have been the subject of a broad interest in the last decade, for both theoretical and experimental scientists, and a considerable effort has been made to characterize the different proposed mechanisms.[1] The excited state proton transfer (ESPT) was first proposed as a responsible mechanism of many biological molecular processes and has been investigated for several prototypical biological-type cluster systems, consisting of a chromophore (phenol, naphthol,...) and basic molecules (ammonia) in a number which reproduces different solvent conditions.[2,3] In these clusters, the chromophore and the solvent are strongly coupled such that the ESPT proceeds adiabatically in a single electronic surface, which has a low barrier for proton transfer.

However, in the last years, this ESPT picture has been challenged and hydrogen-atom transfer (or synchronized proton and electron transfer) has been proposed to account for the excited state dissociation dynamics, in particular, for small molecular systems.[4–6] In a clear parallelism with the H-atom detachment channel in the photodissociation dynamics of bare chromophores, the mechanism for the excited state hydrogen-atom transfer (ESHT) for the molecular complexes was proposed to occur *via* a conical intersection to a higher lying singlet state ($^1\pi\sigma^* \leftarrow {}^1\pi\pi^*$), where the photoexcited chromophore donates a H-atom to the solvation molecules. Ashfold and coworkers have thoroughly characterized this process for a variety of molecules,[7–9] while Sobolewski *et al.* have published a complete theoretical description for bare and solvated systems.[10–14]

The key experiment which disentangled the relevance of the ESPT and ESHT mechanisms on the dynamics of photoexcited clusters was carried out by Pino *et al.*[4,5] on a two-photon, two-colour experiment on phenol–$(NH_3)_3$. They observed that when the experiment was carried out with nanosecond lasers, with a delay time between the pump and the probe pulses of several tens of nanoseconds, the signal corresponding to the $NH_4(NH_3)_2^+$ daughter cluster did not decay. These experiments evidenced the presence of neutral stable $NH_4(NH_3)_2$ species, which cannot be explained in terms of an ESPT process. Proton transfer in the excited state of a parent $PhOH\cdot(NH_3)_n$ cluster should involve the formation of $PhO^{-}{}^*\cdot NH_4^+(NH_3)_{n-1}$ complexes,[5] which upon absorption of a probe UV photon lead to $PhO^\bullet$ and the detected $NH_4^+(NH_3)_{n-1}$ species. The lifetimes of the $PhO^{-}{}^*\cdot NH_4^+(NH_3)_{n-1}$ complexes are in the regime of picoseconds and hence, when a 10 ns delay is introduced between the pump and probe pulses, no signal coming from $NH_4^+(NH_3)_{n-1}$ products should be observed.

Since the work of Pino *et al.* several systems have been studied and ascribed mainly to either ESPT or ESHT, but some controversy, nevertheless, exists. While some authors claim that ESHT is the main responsible mechanism to explain the experimental data, some others argue that it is not possible to rule out any of the two processes without a more deep inspection and additional data.[3]

The photodissociation of bare pyrrole (PyH) constitutes one of the paradigms of mode specific product formation after photoexcitation of medium-sized organic molecules. Pyrrole is a prototypical six π-electron heteroatomic aromatic molecule and constitutes an ideal model for the study of more complex systems, such as nucleobases and aromatic aminoacids.

[a] *Departamento de Química Física I, Facultad de Ciencias Químicas, Universidad Complutense de Madrid, 28040 Madrid, Spain. E-mail: rubio@quim.ucm.es, banares@quim.ucm.es*
[b] *Instituto de Estructura de la Materia, CSIC, C/Serrano, 123, 28006 Madrid, Spain*
[c] *Centro Láser de Ciencias Moleculares – INFIQC, Dpto. de Fisicoquímica, Facultad de Ciencias Químicas, Universidad Nacional de Córdoba, Ciudad Universitaria, Pabellón Argentina, 5000 Córdoba, Argentina*

The UV spectrum—which consists of an intense feature between 165 nm and 210 nm and a weaker one around 240 nm[15,16]—is governed by the interaction of the first excited electronic state S_1 ($^1A_2$, $^1\pi\sigma^*$) with the nearby excited electronic states. The S_1 state of pyrrole presents a 3s Rydberg character for short N–H bond distances, but becomes antibonding when the separation increases.[10,12,17–19] Direct absorption from the S_0 (X^1A_1) ground state to the $^1\pi\sigma^*$ excited state of $^1A_2$ electronic symmetry is electric dipole forbidden, but vibrational coupling to the bound S_2 ($^1B_2$,$^1\pi\pi^*$) state, due to the dominant oscillator strength of the $^1B_2 \leftarrow X^1A_1$ ($\pi^* \leftarrow \pi$) transition, increases the vibronic transition probability. In the classical picture, after absorption to the S_2/S_1 states, the molecule goes back to the ground S_0 state—*via* internal conversion—and, after randomization of the internal energy among the different vibrational degrees of freedom of the molecule, it decomposes into fragments which exhibit statistical energy distributions.

Recently, Sobolewski and coworkers have proposed from theoretical work an alternative and complementary mechanism for the photodissociation of chromophores and nucleobases, involving direct photodissociation in the quasi-dark $^1\pi\sigma^*$ states, resulting in a fast monoenergetic hydrogen atom.[10] Ashfold and coworkers corroborated these theoretical results in a set of experiments on the photodissociation of pyrrole, phenol and imidazole using Rydberg-tagging detection of the formed hydrogen atoms.[7] The kinetic energy distributions (KEDs) of the hydrogen atom showed two separate contributions: a slow and unstructured one explained in terms of the classical picture, and a second one, showing a rich vibrational and resolved activity in the radical co-product. By identifying the active product vibrations, it is possible to determine the specific parent modes that promote the photoexcitation and the subsequent radiationless couplings. The branching ratio between the slow statistical channel and the fast adiabatic channel proved to be strongly dependent on the photolysis wavelength, as well as the vibrational distribution in the radical co-product. The latter remark suggests a notable degree of vibrational adiabaticity in the dissociation of these systems: absorption at a certain photolysis wavelength would promote a particular skeletal mode of the molecule, which would be largely preserved during the parent ($^1\pi\sigma^*$) evolution, acting as a spectator to the N(O)–H bond fission.

The question of how the photochemistry of pyrrole is affected by clustering with protic polar solvents—like H_2O or NH_3—has not been addressed yet, and only some assumptions supported by the comparison with other systems can be made. For example, complexation of phenol by ammonia affects the principal electronic states in different ways. At short O–H bond distances, the $^1\pi\sigma^*$ electronic excited state is stabilized more than the $^1\pi\pi^*$ state, due to its larger dipole moment, resulting in a decrease of the barrier height associated with the $^1\pi\pi^*$–$^1\pi\sigma^*$ curve crossing and favoring the H-atom transfer through the highly repulsive $^1\pi\sigma^*$ state. On the other hand, at longer O–H distances, the S_0 state is stabilized, while the $^1\pi\sigma^*$ state is pushed upwards.[10] As a consequence, the conical intersection between these two states is removed, and therefore, the fast internal conversion (IC) process to the electronic ground state (which is present in the bare molecule) is effectively quenched in the solvated phenol molecule.[10]

In two simultaneous and independent recent papers, the photochemistry of pyrrole–Xe clusters[20] and pyrrole–Ar and $(PyH)_n$ clusters[21] has been theoretically and experimentally investigated. Complexation with Xe or Ar produces a quenching of the fast H-atom elimination channel, while formation of $(PyH)_n$ clusters produces a less noticeable effect, resulting in an inversion of the slow-channel/fast-channel branching ratio. The closing of the adiabatic dissociation channel by the presence of a rare gas atom is explained in terms of a strong shift of the $^1\pi\sigma^*$ curve, which, as in the case of the phenol–ammonia case, would remove the S_0–$^1\pi\sigma^*$ curve crossing while at the same time it would reinforce the Rydberg character of the $^1\pi\sigma^*$ state. The effect of pyrrole clustering is somehow less simple, due to the possibility of having H-atom transfer between an excited pyrrole unit and the surrounding ground state molecules.[21]

Size-controlled cluster experiments employing molecular beams allow us to explore different conditions of microsolvation, opening up the possibility of studying the nature of the hydrogen bonding between pyrrole and the solvent ammonia in a controlled way. The photodynamics of $PyH\cdot(NH_3)_n$ clusters upon excitation with UV light using nanosecond and picosecond laser sources has been one of the last systems studied with the aim to certify the prevalence of the ESHT mechanism over the ESPT mechanism.[22] To the best of our knowledge, this is the only experimental study on this system. The authors of ref. 22 raise the question of which is the leading force in the H-atom transfer on the basis of two different limiting cases: H-atom ejection and a charge-transfer induced proton transfer. The first one starts from the adiabatic mechanism leading to H-atom elimination, as described by Sobolewski *et al.*,[10] and can be understood as a photoinitiated bimolecular reaction. The expelled H-atom collides with the nearest NH_3, being trapped by the $(NH_3)_n$ cluster in the form of an ammonium radical, NH_4. The initial kinetic energy of the ejected H-atom is randomized into the vibrational, rotational and translational degrees of freedom of the $NH_4(NH_3)_m$ ($m = n$–1) radical product. The resultant kinetic energy separates the $NH_4(NH_3)_m$ cluster from the pyrrolyl radical ($Py^\bullet$). The second mechanism implies a reorganization of the charge after electronic excitation. The process starts as an electron transfer, which induces a proton transfer, resulting in the formation of the $Py^\bullet\cdots{}^\bullet NH_4(NH_3)_m$ cluster. The Rydberg-type nature of the $NH_4(NH_3)_m$ radical cluster results in repulsion of the cluster from the pyrrolyl radical. The large values obtained experimentally for the kinetic energies of the $NH_4(NH_3)_m$ radical clusters coincide with the prediction of the coupled-charge transfer mechanism, breaking the parallelism with the photodynamics of the bare molecule, which would imply the H-atom ejection mechanism.[22]

The $PyH\cdot(NH_3)_n$ system has been investigated theoretically only for the cluster with $n = 1$.[22] From the electronic structure calculations, it is suggested that the decomposition reaction which follows UV light absorption should proceed only on the $^1\pi\sigma^*$ potential energy surface, this state being the lowest singlet excited state in PyH. It is reasonably assumed that clustering in this case will affect the $^1\pi\sigma^*$ and S_0 states in a similar way than

in the phenol–ammonia case. However, the fact that the $^1\pi\pi^*$ state lies in energy below the $^1\pi\sigma^*$ will make the photochemistry of the pyrrole–ammonia different from the rest of chromophores. Furthermore, all the interactions between the three main electronic states involved in the photodecomposition dynamics, S_0, S_1 and S_2, would depend on the degree of complexation and so, a straightforward extrapolation of the $PyH{\cdot}NH_3$ system to high order clusters must be carried out carefully.

In this work, we have studied the photodissociation of pyrrole–ammonia clusters using the velocity map imaging (VMI) technique in order to investigate the mechanism of intracluster H-transfer reaction. The present experiments constitute, to the best of our knowledge, the first report on VMI applied to the study of intra-cluster photodynamics of H-bonded systems containing chromophores. The experimental section will focus on the adaptation of the conventional VMI technique to the particular problem of working with H-bonded clusters of aromatic molecules with protic solvents; in the following section, the most relevant results will be shown, to be discussed in the last section, in which the two possible mechanisms for the H-transfer reaction will be analyzed. Finally, the main conclusions will be presented.

II. Experimental

The main characteristics of the experimental setup have been described in detail previously[23] and thus a brief account of the standard procedure employed in this work will be given here, paying special attention to the peculiarities of the present experiment. The whole experiment runs at a repetition rate of 10 Hz. A 0.5–3% mixture of NH_3 and He with a stagnation pressure of 1–1.5 bar passes through a bubbler with pyrrole at room temperature and the mixture is expanded *via* a pulsed nozzle (General Valve Series 9, 0.5 mm diameter orifice) into vacuum. The gas pulse passes through a skimmer (Beam Dynamics, Standard Model 2, 0.5 mm diameter orifice) and reaches the ionization chamber, where the molecular beam is intersected, in the middle of the electrical plates of a time-of-flight mass spectrometer, at right angles by the photolysis and probe laser pulses, which are counter propagated to each other.

The expansion conditions are critical for the formation of H-bonded complexes. In order to attain the best clustering conditions, the pulsed valve was mounted so it was possible to adjust, from outside the reaction chamber without breaking the vacuum, the distance from the valve orifice to the skimmer and the aperture conditions of the valve, while the mass spectrum was monitored *in situ*. Two limiting conditions were characterized, namely the monomer mode and the cluster mode. In the monomer mode, the mass spectra showed no clustering and only monomer species were observed. In the cluster mode, the pulsed valve was adjusted to attain favorable cooling conditions to produce $PyH{\cdot}(NH_3)_n$ clusters with $n \leq 5$. Additionally, $(PyH)_2$ dimers could be observed as well. The concentration of NH_3 present in the gas mixture was a key parameter to characterize the beam, since it affects the relative intensity of the $PyH{\cdot}(NH_3)_n$ and $NH_4(NH_3)_m$ cluster signals. To analyze independently the effect of the cooling and the concentration of NH_3, H-atom detection experiments were carried out both in the cluster and monomer modes using pure He as seeding gas (no NH_3 present). In this situation, the presence of the mass corresponding to the $(PyH)_2$ dimer was the only difference between the two expansion conditions. Fig. 1 shows the Abel inverted VMI images obtained for H-atom detection using a 2 + 1 REMPI scheme at 243.12 nm, using the same laser pulse for photolysis and detection (single-laser, single-color, pump–probe experiment), for the two conditions mentioned above. Due to the high velocity of the H-atom photofragments, the laser bandwidth used to excite the $2s \leftarrow 1s$ H-atom transition is narrower than the Doppler profile. In order to record all velocities with the same probability, the laser was scanned over the Doppler profile of the $2s \leftarrow 1s$ transition during the experiments. The corresponding kinetic energy distributions (KEDs), obtained by angular integration[24] of the images, are shown in Fig. 2. The two components in the KED associated to the well described slow and fast channels in the H-atom elimination of pyrrole[25,26] are clearly apparent. Due to the limitations associated to the single-laser single-color experiments, the characteristic vibrational structure of the fast channel is not resolved. In the cluster mode, the slow component, barely visible at this wavelength for the monomer, grows at the expense of the fast component.

The photolysis laser is the output of a doubled tunable Nd:YAG (Quanta Ray Pro 230) pumped dye laser (Sirah) in the wavelength range 218–240 nm. To generate radiation below 240 nm, a sum-frequency mixing (SFM) unit (Sirah) is used to mix the fundamental radiation of the dye laser with the 355 nm pump coming from the Nd:YAG laser. The probe laser beam is the output of a doubled tunable Nd:YAG (Continuum Surelite SLII-10) pumped dye laser (Continuum ND 60), centered at 333.5 nm with an energy per pulse of 1.5 mJ. The relatively low values of the ionization potentials of the $NH_4(NH_3)_m$ ($m > 2$) radical clusters[27] allow efficient non-resonant ionization with one photon of the 333.5 nm radiation (3.72 eV), while their long lifetimes[28] (of the order of μs) allow the fragments to be ionized using nanosecond pump–probe delays and nanosecond laser pulses. The NH_4 and NH_3NH_4 products are characterized by ionization potentials above 3.72 eV, and thus no single probe photon ionization of these species is produced. On the other hand, the lifetime of NH_4 is so short (15 ps) that a pump–probe detection of this species is only possible if both the laser pulses overlap in time. We have used these two facts to check that multiphoton processes do not participate in our results.

Since the first experiments on the photodissociation of CH_3I,[29] the VMI technique has become an essential tool for the study of photodissociation dynamics of a great variety of molecular systems,[30] which strikingly do not include cluster decomposition by photoinduced H-atom and/or proton transfer reactions. As it concerns to dissociation of clusters of biological interest, the VMI technique has been applied only recently to measure the binding energies of benzene–water and difluorobenzene–water systems.[31] It has been used, as well, to study the effect of clustering with rare gases on the photodecomposition of bare chromophores.[20]

The imaging experiments presented here have been performed in a recently improved single field VMI set up. In the single field configuration, only two electrodes are used. Unlike previous velocity mapping and slicing methods, where the focusing condition is obtained by adjusting the voltage on

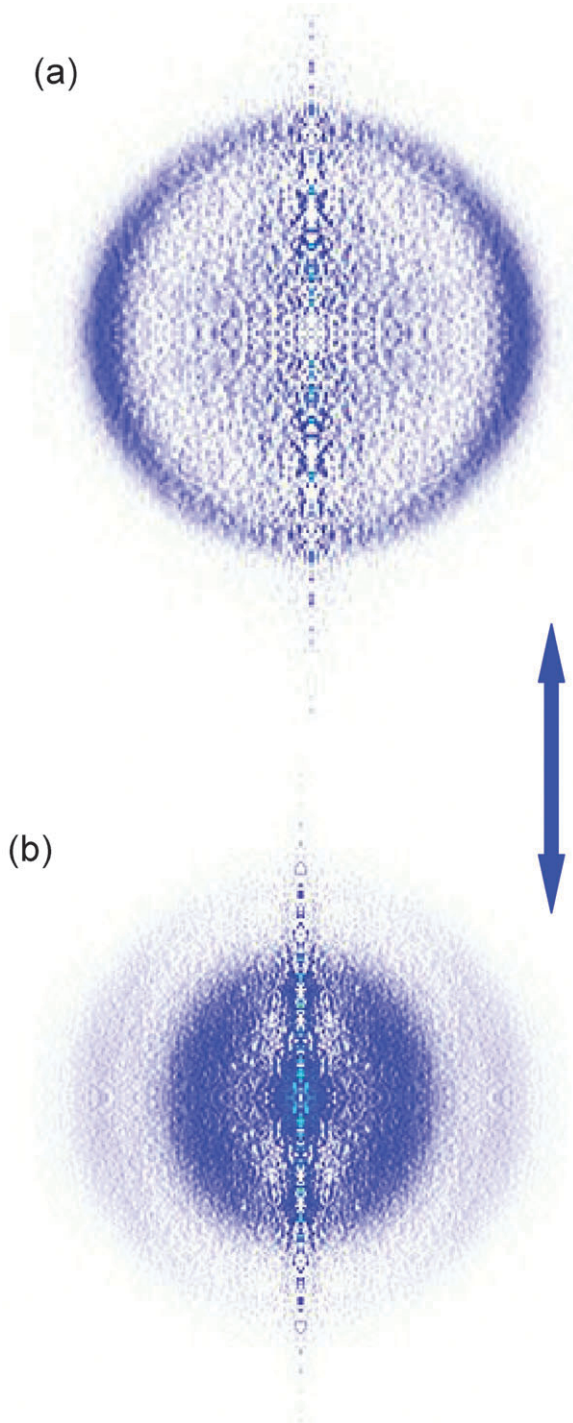

Fig. 1 H-atom images obtained from the photodissociation of bare pyrrole (PyH) at 243.2 nm. (a) Abel-inverted image for the PyH monomer photodissociation. (b) Abel-inverted image for the $(PyH)_2$ dimer photodissociation. The experiment was carried out using a single laser/single color for photolysis and detection of H-atoms through a 2 + 1 REMPI scheme at 243.12 nm, corresponding to the 2s ← 1s transition of H. The double-headed arrow denotes the polarization direction of the laser pulses.

the second field ion lens, in the single field configuration the focusing condition is met when the starting position along the time-of-flight (TOF) axis is at a specific distance from either the repeller or the extractor.[32]

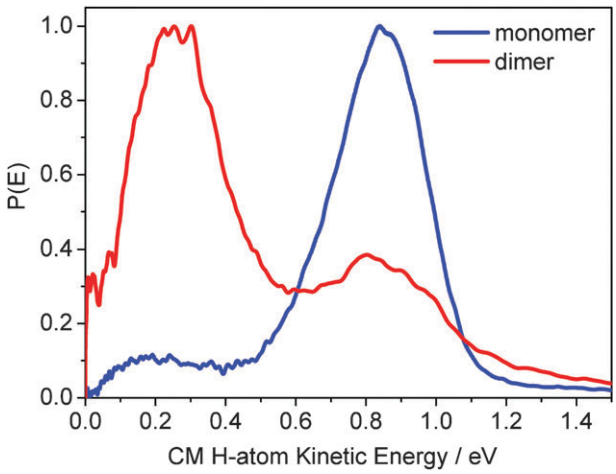

Fig. 2 Center-of-mass (CM) H-atom kinetic energy distributions obtained by integration of the images shown in Fig. 1. The blue curve corresponds to the expansion conditions where only monomer species are detected. The red curve corresponds to the cluster (dimer) conditions. The distributions are normalized arbitrarily to have the same overall intensity.

The vast majority of cluster photodissociation experiments documented so far employ unfocused laser irradiation in order to minimize molecular fragmentation. In the traditional Wiley–McLaren TOF configuration, the velocity mapping conditions for the resultant large molecular beam–laser interaction region are attained adjusting the ion optics voltages for each particular experiment. In contraposition, the single field configuration, although proven to allow at least just as good product speed resolution as conventional VMI techniques, is more sensitive to the spread of the ion cloud in the TOF axis direction, which occurs when using unfocused laser beams. In the present work, different focusing conditions of the pump and probe lasers have been explored, having to fulfill the condition of minimum molecular fragmentation without a significant decrease in resolution. To check the latter, a pump–probe photodissociation experiment on CH_3I, with the photolysis laser centered at 230 nm and the probe laser centered at 333.45 nm to detect $CH_3(\nu = 0)$ products by 2 + 1 REMPI,[33] has been carried out for several focusing configurations. Fig. 3 shows a raw $CH_3(\nu = 0)$ image and the corresponding radial velocity distribution (in pixels) obtained for the preferred configuration. For comparison purposes, the velocity distribution obtained in usual focusing conditions at the same photolysis and probe wavelengths is overlaid. Three main features are observed in the image, namely, pump–probe middle and outer rings corresponding to the $CH_3(\nu = 0)$ + $I^*(^2P_{1/2})$ and $CH_3(\nu = 0)$ + $I(^2P_{3/2})$ channels, respectively, for photolysis at 230 nm, and an inner ring corresponding to the $CH_3(\nu = 0)$ + $I(^2P_{3/2})$ channel for photolysis by the probe laser at 333.45 nm. This latter signal arising from the one-color probe-laser experiment was not completely minimized in order to check as well the influence of the focusing conditions of the probe laser beam. The focusing conditions employed were the following: the unfocused pump laser was strongly collimated and cleaned in order to have a spot size of about 1 mm^2 of homogeneous intensity ($\sim$15 mJ cm^{-2}); the probe laser was loosely focused, setting a 60 cm focal length lens slightly out of

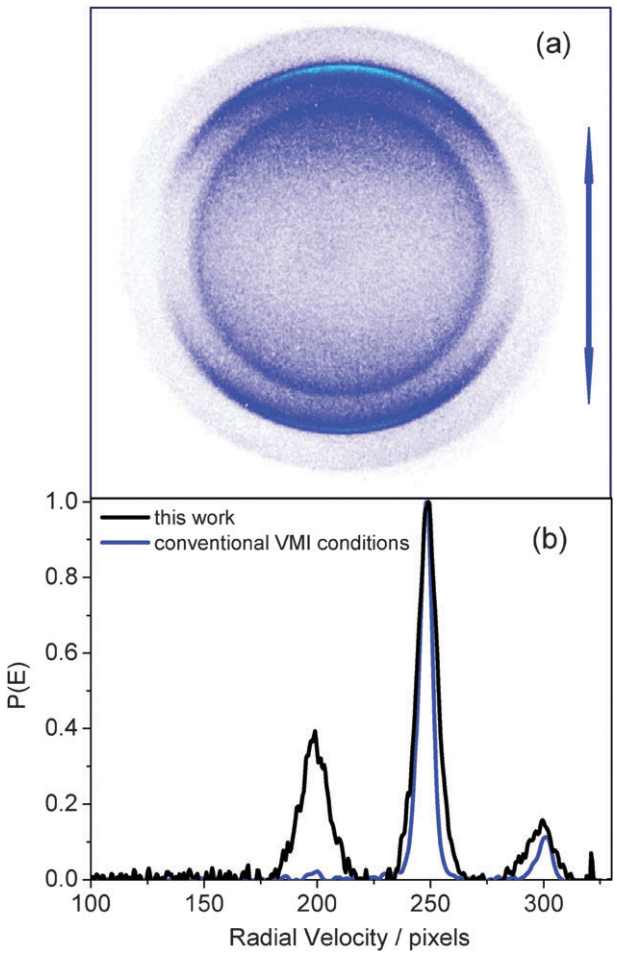

Fig. 3 (a) Raw image of the $CH_3(\nu = 0)$ ion fragment arising from the CH_3I photodissociation at 226 nm and probing $CH_3(\nu = 0)$ fragments by 2 + 1 REMPI at 333.5 nm in the focusing conditions employed in the photodissociation of $PyH{\cdot}(NH_3)_n$ clusters. (b) Radial velocity distribution (in pixels) obtained from the integration of the image (black line). The velocity distribution obtained in conventional focusing conditions for VMI is also included for comparison (blue line). The double-headed arrow denotes the polarization direction of both pump and probe laser pulses.

focus. It is clearly seen in Fig. 3 that the softening of the focusing conditions involves an increase of the width of the features in the velocity distribution. To estimate the decrease of resolution, a Gaussian fit of the $I^*(^2P_{1/2})$ peak has been carried out in both curves (not shown). The full-width-half-maximum (FWHM) of the Gaussian fit for the usual laser focusing conditions is $\sim$7 pixels, which means a relative velocity resolution of 2.8%. This value is increased to 4.4% for the focusing conditions employed in this work, and thus, there is a decrease of less than 2% in resolution. Furthermore, the VMI technique is ideal to study those systems in which the product translational energy is small, like the one studied in the present work, because the image absolute resolution is linear in velocity, and so the energy resolution is higher at low translational energies.

It is important to notice that even though our current experimental setup has the capability to work using the slice imaging technique,[34] in the present case we have operated the mass spectrometer in the conventional VMI mode, which can be performed without alterations in our imaging machine. In the delayed pulse extraction slice imaging technique, a certain time delay between the arrival of the probe laser and the trigger, which sets on the repeller voltage, has to be applied for the ion cloud to expand before collection. The time delay applied to the extraction must be chosen to allow the ion cloud to expand several hundreds of nanoseconds, so as to be sliced by a narrow time gate at the detector. Usual extraction delays span the range of 200 to 600 ns. Due to the small velocity recoil of the $NH_4(NH_3)_m$ product clusters, if total slicing had to be attained, the extraction delay should surpass these values significantly. At the maximum delay checked, $\Delta\tau = 1$ μs, the expansion of the ion cloud was not enough to perform a good quality slicing, but at the same time, the image was already distorted due to a mismatch of the autofocusing condition caused by the stretching of the ion spot along the TOF axis direction, as discussed before. The current experiment constitutes, therefore, a critical case in which slicing is not appropriate. VMI reconstructed images present a vertical centre-line noise artificially introduced by the reconstruction method. In order to certify that this noise does not distort the experimental results, additionally angular integrations of the recorded images excluding the poles have been carried out. The resulting kinetic distributions are indistinguishable from those presented here.

The accelerated ions pass through a field-free TOF region before hitting impedance matched MCPs (Chevron configuration, 40 mm diameter). The MCPs can be gated with a high voltage pulse to allow only the ions of interest to be detected. The resulting electron avalanche strikes a phosphor screen (P47), thereby creating the ion image, which is recorded by a CCD camera (SONY 1024 × 768 pixel) controlled by National Instruments (NI) LABVIEW 7.1 and IMAQ VISION software. The final image is obtained as the sum of around 20 000–100 000 laser shots, depending on the quality of the signal.

Fig. 3 has been employed to calibrate the detector as well. The relation between the kinetic energy (E_k) of any fragment and the distance to the center of the detector at which it appears (in pixels) depends on the electric voltage applied (V), the length of the time-of-flight region (L), and the charge of the particle (q) through the following relation:

$$E_k(\text{fragment}) = \frac{L^2}{qV} \times \text{pixel}^2 = k \times \text{pixel}^2 \qquad (1)$$

where k is a calibration constant, which does not depend on the mass of the fragment detected. This relation allows the transformation of the x-axis of the velocity distribution into center-of-mass (CM) kinetic energy, without any previous knowledge of the photodynamics of the process.[35]

III. Results

The energetic threshold for the ESHT process has been examined in the mass spectrum for three different product species, namely $NH_4(NH_3)_m$, m = 2 to 4, recorded at a fixed probe wavelength of 333.5 nm, while the photolysis laser was scanned between 234 nm and 237 nm (action spectrum).

The results, depicted in Fig. 4, show a smooth transition at around 236.6 nm, in agreement with the experiments of David *et al.*[22] In the photodissociation of bare pyrrole, the adiabatic N–H bond rupture (fast channel) has been observed to occur between 254 nm and 225 nm.[9] The fact that the H-atom transfer process in the PyH·$(NH_3)_n$ clusters is observed at higher energies in comparison with bare pyrrole is related directly to the change in the photodynamics induced by solvation, and it will be discussed in more detail in the following section.

The mass spectra recorded at all photolysis wavelengths employed in the present study show a similar structure. Fig. 5 shows the mass spectra measured at the photolysis wavelength of 226 nm at two delay times between the photolysis and probe laser pulses. The conditions were set such that no signal could be detected from each laser individually. At zero delay time, there are two regions clearly distinguishable. For masses smaller than 45 amu, the mass spectrum is somehow congested due to a relatively large fragmentation of the species present in the molecular beam. In the higher-mass region, the mass spectrum is structured in a progression of the PyH·$(NH_3)_n$ (n = 1–5) parent species. However, for a delay time of 30 ns, only the $NH_4(NH_3)_{n-1}$ products are visible, indicating that the signals associated to fragmentation and to the parent species are produced by simultaneous absorption of pump and probe photons. These results are in good agreement with those obtained by David *et al.*[22] and thus confirm that we are dealing with an ESHT process and not with ESPT, nor reactions in ionized clusters.

VMI images were taken by setting the detector gate in each mass of the different product species. A typical raw image, corresponding to $NH_4(NH_3)_2$ at a photolysis wavelength of 226 nm, is shown in Fig. 6. The images recorded for all the fragments show a similar pattern: a small isotropic feature corresponding to fragments of very small velocity recoil.

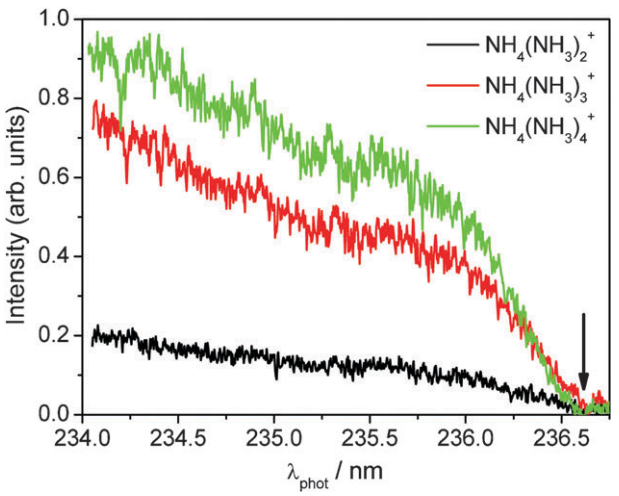

Fig. 4 Action spectra recorded for the $NH_4(NH_3)_m$ products with m = 2, 3 and 4 while scanning the photolysis laser. The detection wavelength was set to 333.5 nm, and the three products were recorded simultaneously from the mass spectrum. The vertical arrow indicates the threshold wavelength of 236.6 nm for the appearance of product ammonia clusters.

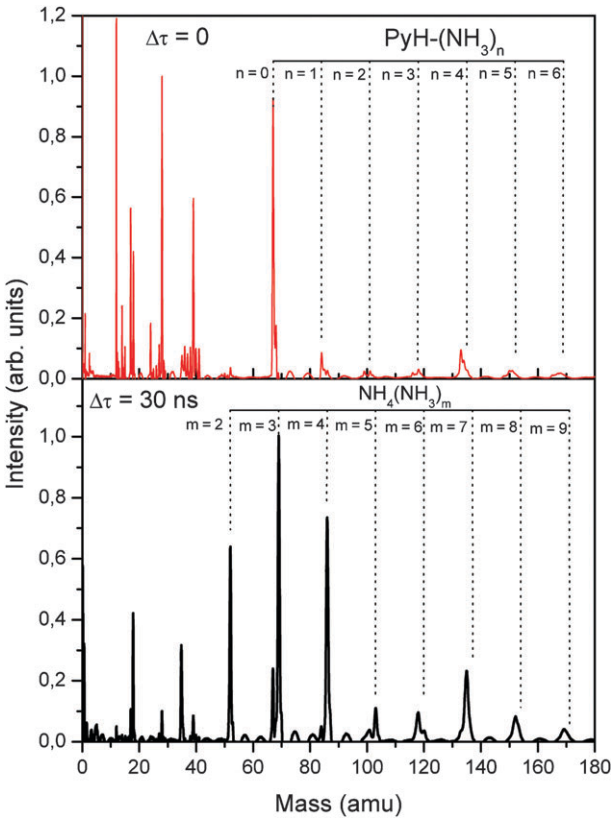

Fig. 5 Pump-and-probe time-of-flight mass spectra obtained at the photolysis wavelength of 226 nm. The zero delay time spectrum (upper panel) shows the contribution of fragmentation and the parent PyH·$(NH_3)_{n=1-6}$ progression. When a delay photolysis wavelength of 30 ns is introduced, only the products $NH_4(NH_3)_{n-1}$ signal is observed.

Images corresponding to the parent clusters were recorded as well (not shown) to compare the relative radius of non-recoiling signals with those of the fragments. As expected, the images of neutral species integrated in the molecular beam are round spots of a few (5 to 10) pixels of diameter. The dotted circles depicted in Fig. 6 denote the hypothetical hitting positions in the detector of fragments with CM kinetic energies of 0.5 eV (outer) and 0.12 eV (inner). The first value corresponds to the experimental energy for the $NH_4(NH_3)_2$ product reported by David *et al.*,[22] while the second limits the signal obtained in this work for the same species.

Fig. 7 shows the KEDs obtained by integration of the images corresponding to the fragment $NH_4(NH_3)_2$ taken at the different photolysis wavelengths employed in the present study. As can be seen, all the distributions show a similar profile consisting of very slow Boltzmann-like envelope with a well resolved structure around the maximum (sited at ~0.01 eV), and a tail lasting several tens of meV. A narrowing of the distributions is observed as the photolysis wavelength increases, in accord with a reduction of the total available energy. Fig. 8 shows the KEDs corresponding to the fragments $NH_4(NH_3)_m$ for m = 2, 3, 4 at the fixed photolysis wavelength of 220 nm. The distributions present the same main features in all cases, but the vibrational structure appears significantly blurred due to the larger masses.

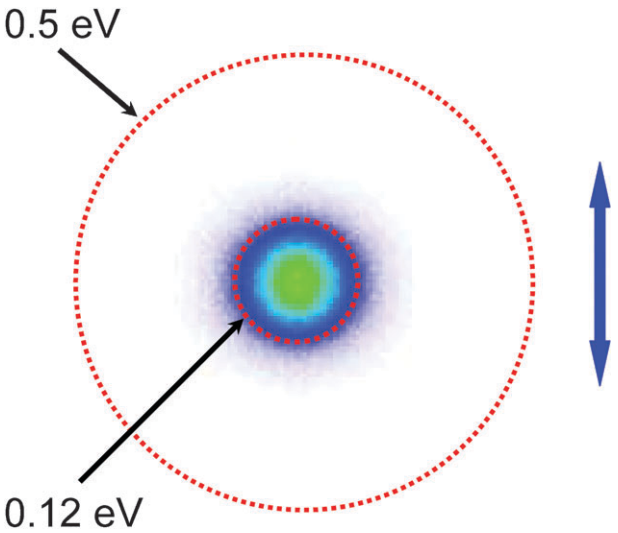

Fig. 6 VMI raw image corresponding to $NH_4(NH_3)_2$ products formed in the photodissociation of $PyH{\cdot}(NH_3)_n$ at a photolysis wavelength of 226 nm. The outer dotted circle denotes the position of the detector where fragments with kinetic energy of 0.5 eV (according to ref. 22) should appear. The position of the inner circle coincides with the maximum value of the scale in Fig. 7 and 8 at 0.12 eV. The double-headed arrow denotes the polarization direction of both pump and probe laser pulses.

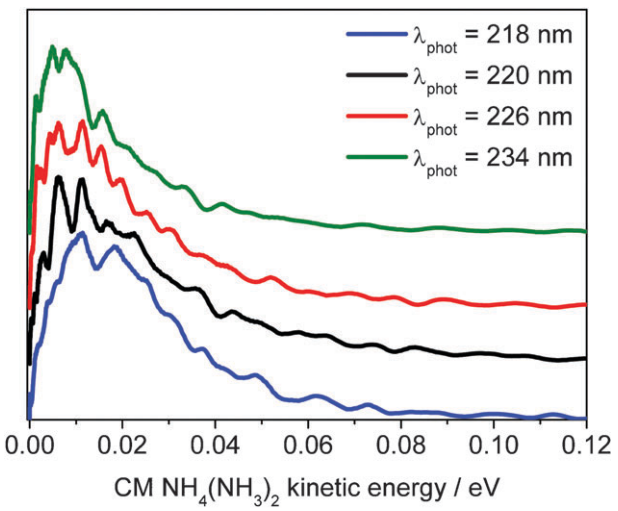

Fig. 7 Kinetic energy distributions obtained by integration of the images corresponding to the $NH_4(NH_3)_2$ fragment taken at the different photolysis wavelengths employed in the present study. The distributions have been vertically shifted for a clear comparison. The maximum value in the energy axis corresponds to the inner dotted circle in Fig. 6.

IV. Discussion

It has been shown before in photodissociation studies of bare pyrrole that the H-atom elimination channel does not show any barrier in the photolysis wavelength (λ_{phot}) range between 193 nm and 254 nm.[26] At wavelengths larger than 240 nm, the well resolved structure in the H-atom KED corresponding to the fast channel indicates that the absorption at these wavelengths is induced by vibrational coupling. At higher energies, the slow

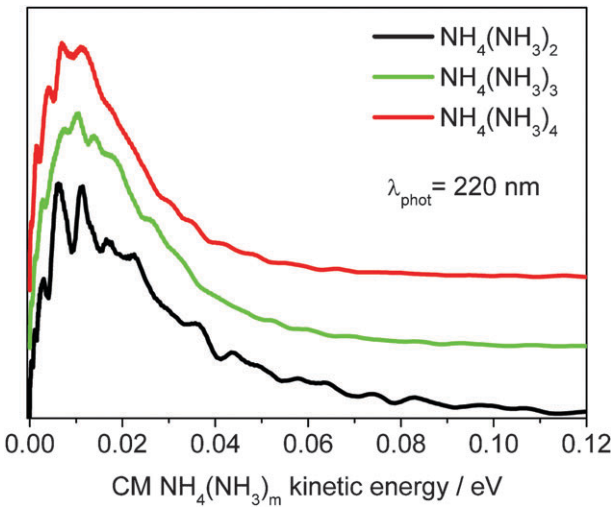

Fig. 8 Kinetic energy distributions obtained by integration of the images corresponding to the $NH_4(NH_3)_m$ for $m = 2, 3, 4$ fragments at a fixed photolysis wavelength of 220 nm. The distributions have been vertically shifted for a clear comparison. The maximum value in the energy axis corresponds to the inner dotted circle in Fig. 6.

channel gains in intensity, while the KED of the fast channel loses the sharp structure. Therefore, when λ_{phot} is reduced from 240 nm to 193 nm, the additional energy provided by the photon is largely retained as vibrational excitation of the pyrrolyl moiety. The fact that a clear barrier is measured for the $PyH{\cdot}(NH_3)_n$ system indicates that the vibrationally-induced absorption mechanism is largely affected by the solvating ammonia.

The KEDs measured in the present work shown in Fig. 7 and 8 do not match with the mechanism proposed by David *et al.* for the H-atom transfer process, in which a long-lived intermediate state is invoked.[22] In their experiments, they used a conventional Wiley–McLaren time-of-flight mass spectrometer improved with pulsed extraction. In order to have kinetic energy resolution, the delay between the extraction pulse and the laser pulses were of the order of few microseconds. In the work of David *et al.*, the high kinetic energies measured for the reaction products break the parallelism between the photodissociation mechanism of the bare molecule, based on a direct H-atom elimination, and the corresponding mechanism for photodissociation of the pyrrole–ammonia clusters.[22] On the other hand, the product kinetic energies obtained in the present work (see Fig. 7) largely disagree with the values reported by David *et al.*, and moreover, they constitute a reinforcement of the impulsive model as the mechanism for pyrrole–ammonia clusters photodissociation.

The energy balance for the photodissociation of bare pyrrole is given by:

$$E_k(H) = \frac{m_{Py}}{m_{PyH}}[h\nu - D_0 - E_{vib}(Py)] \qquad (2)$$

where E_k is the center-of-mass (CM) kinetic energy of the H-atom, ν is the frequency of the photolysis laser, D_0 = 4.073 eV is the dissociation energy of the N–H bond,[26] m_{Py} and m_{PyH} are the masses of pyrrolyl radical and pyrrole,

respectively, and $E_{vib}(Py)$ is the vibrational energy of the pyrrolyl co-fragment. Since the experiment does not possess rotational resolution, the rotational energy of the pyrrolyl radical is introduced as a broadening of the vibrational bands. Following eqn (2), the H-atom KED is discretized due to the $E_{vib}(Py)$ term, where the maximum possible kinetic energy of the H-atom (the available energy) is given by:

$$E^{av}(H) = \frac{m_{Py}}{m_{PyH}}[h\nu - D_0] \quad (3)$$

In the impulsive model, the H-atom transfer is regarded as a reactive collision between the ejected H-atom and the ammonia cluster solvent. The kinetic energy of the ammonia cluster product will be obtained assuming the momentum conservation rule when no vibrational excitation is produced due in the collision process:

$$m_H\vec{v}_H + m_{(NH_3)_n}\vec{v}_{(NH_3)_n} = m_{NH_4(NH_3)_{n-1}}\vec{v}_{NH_4(NH_3)_{n-1}} \quad (4)$$

where the maximum speed of the H-atom is given by $v_H = \sqrt{\frac{2E^{av}(H)}{m_H}}$. Assuming zero velocity for the ammonia clusters in the molecular beam, the available energy for the ammonia cluster products (*i.e.* their maximum kinetic energy) is straightforward derived from eqn (4) as:

$$E^{av}[NH_4(NH_3)_m] = \frac{m_H}{m_{NH_4(NH_3)_m}}E^{av}(H) \quad (5)$$

Note that the available energy for the $NH_4(NH_3)_{m=n-1}$ cluster products produced by an electronic ESHT mechanism would be given by:

$$E^{av}[NH_4(NH_3)_{n-1}] = \frac{m_{Py}}{m_{PyH\cdot NH_4(NH_3)_n}}[h\nu - D_0] \quad (6)$$

Using eqn (5), the available energy for the $NH_4(NH_3)_m$ fragments is calculated for each photolysis wavelength. Fig. 9 shows the KEDs of nascent $NH_4(NH_3)_2$ depicted in Fig. 7, but normalized to the available energy given by eqn (5). According to the impulsive mechanism, any structure in the normalized $NH_4(NH_3)_m$ fragment KEDs should reflect the vibrational activity of the pyrrolyl radical. Taking as input the position of the peaks in the measured normalized $NH_4(NH_3)_m$ fragment KEDs, the vibrational energies of the pyrrolyl radical can be calculated using backwards eqn (5) to (2). The spacing between the major features in the cluster products KEDs suggests that there are two main vibrational modes of the pyrrolyl radical involved, with energies around 3000 cm^{-1} and 1500 cm^{-1}. There are several vibrational modes of a_1 and b_2 symmetry—in Herzberg's notation[36]—compatible with these values. The electric dipole selection rules ensure that the initial excitation can only populate levels of a_2, b_1 and b_2 vibrational symmetry, which reduces the possibilities to ν_{12} = 3226 cm^{-1} and ν_{13} = 3193.9 cm^{-1} on one hand, and ν_{14} = 1355.8 cm^{-1} or even ν_{15} = 1291.6 cm^{-1} on the other. Combination modes of appropriate symmetry cannot be ruled out either.[9] In order to decipher the structure appearing in Fig. 7–9, and without the aim to perform any accurate assignment, the vibrational combs for the modes ν_{12} and ν_{14} of the pyrrolyl radical are represented in Fig. 9.

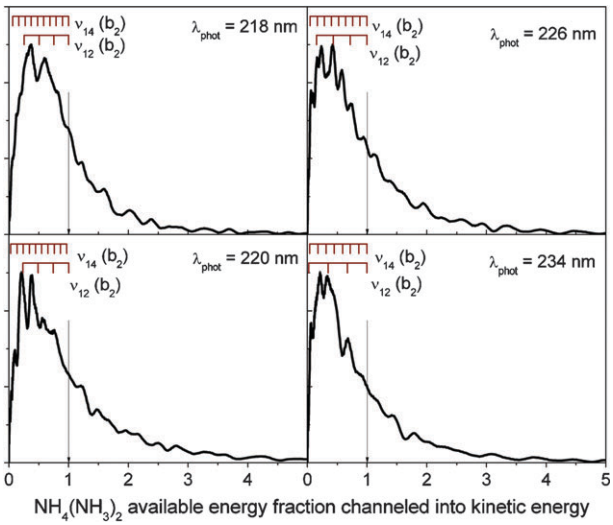

Fig. 9 Detailed kinetic energy distributions for the $NH_4(NH_3)_2$ products at the different photolysis wavelengths employed in the present study. In the abscissas, the $NH_4(NH_3)_2$ product available energy fraction channelled into kinetic energy is represented. The arrow indicates the kinetic energy correlating to species with zero internal energy. The observed structure is related to the vibrational activity of the pyrrolyl radical. The combs in the top part of each panel correspond to the vibrational quantum states of the ν_{12} and ν_{14} modes of the pyrrolyl co-fragment moiety. The tail in the KED extending towards values larger than one is related to internal energy of the ammonia clusters.

Despite the observed similarities with the photodissociation of bare pyrrole, there is a remarkable difference related to the promoting modes involved in the absorption. In the work of Ashfold and co-workers on the photodissociation of pyrrole,[9] the vibrational modes observed had energies below 1400 cm^{-1}, taking values as low as 700 cm^{-1}. Moreover, only a single quantum of each mode was observed in the H-atom KEDs. The interpretation of our experimental results assumes an elevated amount of vibrational energy in the pyrrolyl radical, being considerably larger than in the case of the photodissociation of bare pyrrole.

For the following discussion, it is assumed that analogous energy shifts happen in the phenol–ammonia and the pyrrole–ammonia systems for the excited $^1\pi\pi^*$ and $^1\pi\sigma^*$ states. However, the key point stands on the differences between these two systems. While in the phenol–ammonia clusters the stabilization of the $^1\pi\sigma^*$ state results in a lowering of the $^1\pi\pi^*$–$^1\pi\sigma^*$ barrier [10] (as it happens for the clusters between ammonia and most of the chromophores), in pyrrole the $^1\pi\sigma^*$ state lies below in energy than the $^1\pi\pi^*$ state and, hence, the stabilization of the $^1\pi\sigma^*$ state would result in an increase of the $^1\pi\pi^*$–$^1\pi\sigma^*$ gap. As a consequence, the energy coupling necessary for the absorption to the $^1\pi\sigma^*$ state would involve higher vibrational sub-levels in the case of pyrrole. Additionally, the absorption range would be reduced, or at least, shifted to lower wavelengths, which agrees with the observed barrier around 236.6 nm. Due to the remarkable degree of vibrational adiabaticity in the dissociation of pyrrole molecules through their ^1S ($^1A_2$, $^1\pi\sigma^*$) state, the pyrrolyl radical should show a correlated high vibrational activity, in concordance with our experimental results.

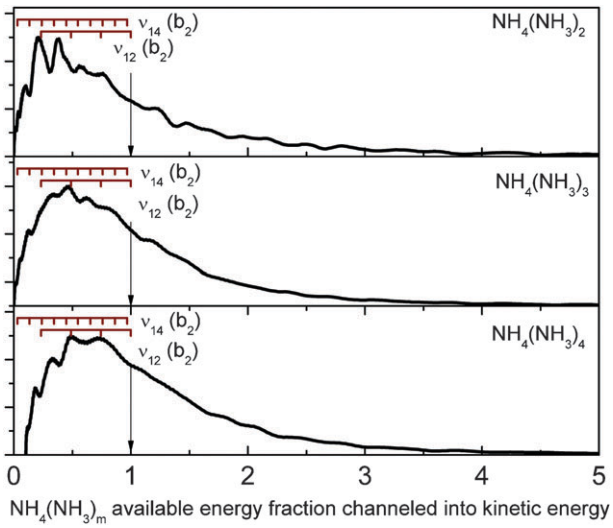

Fig. 10 Detailed kinetic energy distributions for the $NH_4(NH_3)_m$ for $m = 2, 3, 4$ fragments at a fixed photolysis wavelength of 220 nm. In the abscissas, the $NH_4(NH_3)_m$ product available energy fraction channelled into kinetic energy is represented. The arrow indicates the kinetic energy correlating to species with zero internal energy. The observed structure is related to the vibrational activity of the pyrrolyl radical. The combs in the top part of each panel correspond to the vibrational quantum states of the ν_{12} and ν_{14} modes of the pyrrolyl co-fragment moiety. The tail in the KED extending towards values larger than one is related to internal energy of the ammonia clusters.

The tail extending towards values of the $NH_4(NH_3)_2$ available energy fraction channelled into kinetic energy larger than one in the KEDs shown in Fig. 9 corresponds to the vibrational energy of the $(NH_3)_n$ "parent" clusters, which is responsible, as well, for the partial blurring of the vibrational structure. Accordingly, the blurring increases with the size of the $(NH_3)_n$ cluster (see Fig. 7). The available energy for the $NH_4(NH_3)_m$ products depends on the cluster mass, but once the kinetic energy is normalized to the available energy for a particular wavelength, the vibrational structure does not depend on it, and each vibrational feature (peak) should have a match in every ammonia cluster KED. The corresponding KEDs of the $NH_4(NH_3)_m$ ($m = 2, 3, 4$) normalized to the available energy at a photolysis wavelength of 220 nm (Fig. 10) clearly show that the well resolved peaks of the $NH_4(NH_3)_2$ KED have a correspondence in the other two species $NH_4(NH_3)_3$ and $NH_4(NH_3)_4$.

V. Conclusions

Velocity map imaging experiments have been carried out to study the photodynamics of the hydrogen transfer reaction in pyrrole–ammonia clusters of different sizes through non-resonant ionization detection of the $NH_4(NH_3)_{m=2-4}$ radical products. The kinetic energy released into the products is explained in terms of an impulsive mechanism, in which the hydrogen transfer reaction starts as an adiabatic photodissociation of pyrrole (fast H-atom channel) followed by a collision of the H-atom with the $(NH_3)_n$ solvent cluster. This interpretation is in disagreement with the work of David *et al.*,[22] but follows previous analysis on the phenol–ammonia and similar chromophore–ammonia systems. The product kinetic energy distributions measured in the present work show a structure which is associated to a discrete velocity distribution of the colliding H-atom which, in turn, reflects the vibrational activity of the pyrrolyl radical, formed in the photodissociation step.

Acknowledgements

We are grateful to Professor T. N. Kitsopoulos for his help to implement the single field velocity mapping technique in our laboratory. L.R.-L. thanks Consejo Superior de Investigaciones Científicas (CSIC) for a JAE-DOC contract under the Unidad Asociada "Química-Física Molecular" between Departamento de Química Física I of Universidad Complutense and CSIC. This work has been supported by AECI, Spanish Ministry of Foreign Affairs, project A/7763/07, and by the Spanish Ministry of Science and Innovation through grants CTQ2008-02578/BQU and Consolider Program SAUUL CSD2007-00013. The facilities provided by the Centro de Asistencia a la Investigación de Espectroscopia Multifotónica y de Femtosegundo (UCM) are gratefully acknowledged.

References

1 I. V. Hertel and W. Radloff, *Rep. Prog. Phys.*, 2006, **69**, 1897.
2 O. David, C. Dedonder-Lardeux and C. Jouvet, *Int. Rev. Phys. Chem.*, 2002, **21**, 499, and references therein.
3 R. Knochenmuss and I. Fischer, *Int. J. Mass Spectrom.*, 2002, **220**, 343.
4 G. Pino, C. Dedonder-Lardeux, G. Grégoire, C. Jouvet, S. Martrenchard and D. Solgadi, *J. Chem. Phys.*, 1999, **111**, 10747.
5 G. Pino, G. Grégoire, C. Dedonder-Lardeux, C. Jouvet, S. Martrenchard and D. Solgadi, *Phys. Chem. Chem. Phys.*, 2000, **2**, 893.
6 G. Grégoire, C. Dedonder-Lardeux, C. Jouvet, S. Martrenchard, A. Peremans and D. Solgadi, *J. Phys. Chem. A*, 2000, **104**, 9087.
7 M. N. R. Ashfold, B. Cronin, A. L. Devine, R. N. Dixon and M. G. D. Nix, *Science*, 2006, **312**, 1637.
8 M. G. D. Nix, A. L. Devine, B. Cronin and M. N. R. Ashfold, *J. Chem. Phys.*, 2006, **125**, 133318.
9 B. Cronin, M. G. D. Nix, R. H. Qadiry and M. N. R. Ashfold, *Phys. Chem. Chem. Phys.*, 2004, **6**, 5031.
10 A. L. Sobolewski, W. Domcke, C. Dedonder-Lardeux and C. Jouvet, *Phys. Chem. Chem. Phys.*, 2002, **4**, 1093.
11 A. L. Sobolewski and W. Domcke, *Chem. Phys. Lett.*, 1999, **315**, 293.
12 A. L. Sobolewski and W. Domcke, *Chem. Phys.*, 2000, **259**, 181.
13 A. L. Sobolewski and W. Domcke, *J. Phys. Chem. A*, 2001, **105**, 9275.
14 A. L. Sobolewski, W. Domcke, C. Dedonder-Lardeux and C. Jouvet, *Phys. Chem. Chem. Phys.*, 2002, **4**, 1093.
15 P. A. Mullen and M. K. Orloff, *J. Chem. Phys.*, 1969, **51**, 2276.
16 M. Bavia, F. Bertinelli, C. Taliani and C. Zauli, *Mol. Phys.*, 1976, **31**, 419.
17 M. H. Palmer, I. C. Walker and M. F. Guest, *Chem. Phys.*, 1998, **238**, 179.
18 B. O. Roos, P. A. Malmqvist, V. Molina, L. Serrano-Andres and M. Merchan, *J. Chem. Phys.*, 2002, **116**, 7526.
19 J. Wan, J. Meller, M. Hada, M. Ehara and H. Nakatsujia, *J. Chem. Phys.*, 2002, **113**, 7853.
20 L. Rubio-Lago, D. Zaouris, Y. Sakellariou, D. Sofikitis, T. N. Kitsopoulos, F. Wang, X. Yang, B. Cronin, A. L. Devine, G. A. King, M. G. D. Nix, M. N. R. Ashfold and S. S. Xantheas, *J. Chem. Phys.*, 2007, **127**, 064306.
21 V. Poterya, V. Profant, M. Fárnik, P. Slavicek and U. Buck, *J. Chem. Phys.*, 2007, **127**, 064307.
22 O. David, C. Dedonder-Lardeux, C. Jouvet, H. Kang, S. Martrenchard, T. Ebata and A. L. Sobolewski, *J. Chem. Phys.*, 2004, **120**, 10101.

23 L. Rubio-Lago, A. García-Vela, A. Arregui, G. A. Amaral and L. Bañares, *J. Chem. Phys.*, 2009, **131**, 174309.
24 *Imaging in Molecular Dynamics*, ed. B. J. Whitaker, Cambridge University Press, 2003.
25 J. Wei, A. Kuczmann, J. Riedel, F. Renth and F. Temps, *Phys. Chem. Chem. Phys.*, 2003, **5**, 315.
26 B. Cronin, M. G. D. Nix, R. H. Qadiri and M. N. R. Ashfold, *Phys. Chem. Chem. Phys.*, 2004, **6**, 5031.
27 K. Fuke, R. Takasu and F. Misaizu, *Chem. Phys. Lett.*, 1994, **229**, 597.
28 K. Fuke and R. Takasu, *Bull. Chem. Soc. Jpn.*, 1995, **68**, 3309.
29 D. W. Chandler and P. L. Houston, *J. Chem. Phys.*, 1987, **87**, 1445.
30 M. N. R. Ashfold, N. H. Nahler, A. J. Orr-Ewing, P. J. Vieuxmaire, R. L. Toomes, T. N. Kitsopoulos, I. A. Garcia, D. A. Chestakov, S. Wu and D. H. Parker, *Phys. Chem. Chem. Phys.*, 2006, **8**, 26.
31 S. M. Bellm, J. R. Gascooke and W. D. Lawrance, *Chem. Phys. Lett.*, 2000, **330**, 103; R. K. Sampson, S. M. Bellm, J. R. Gascooke and W. D. Lawrance, *Chem. Phys. Lett.*, 2002, **372**, 307.
32 V. Papadakis and T. N. Kitsopoulos, *Rev. Sci. Instrum.*, 2006, **77**, 083101.
33 A. T. J. B. Eppink and D. H. Parker, *J. Chem. Phys.*, 1999, **110**, 832.
34 C. R. Gebhardt, T. P. Rakitzis, P. C. Samartzis, V. Ladopoulos and T. N. Kitsopoulos, *Rev. Sci. Instrum.*, 2001, **72**, 3848.
35 A. T. J. B. Eppink and D. H. Parker, *Rev. Sci. Instrum.*, 1997, **68**, 3477.
36 G. Herzberg, *Molecular Spectra and Molecular Structure. III Electronic Spectra and Electronic Structure of Polyatomic Molecules*, van Nostrand, New York, 1966.